Materials Today Bio 24 (2024) 100934

Contents lists available at ScienceDirect

Materials Today Bio

journal homepage: www.journals.elsevier.com/materials-today-bio

Integrated evaluation of biomechanical and biological properties of the biomimetic structural bone scaffold: Biomechanics, simulation analysis, and osteogenesis

Jialiang Li [a,*], Yubing Yang [b], Zhongwei Sun [c], Kan Peng [a], Kaixin Liu [a], Peng Xu [a], Jun Li [a], Xinyu Wei [d], Xijing He [b]

[a] Honghui Hospital, Xi'an Jiaotong University, Xi'an, 710014, China
[b] Department of Orthopedics, The Second Affiliated Hospital of Xi'an Jiaotong University, Xi'an, 710000, China
[c] Jiangsu Key Laboratory of Engineering Mechanics, School of Civil Engineering, Southeast University, Nanjing, 210096, China
[d] Department of Health Management, The Second Affiliated Hospital of Xi'an Jiaotong University, Xi'an, 710000, China

ARTICLE INFO

Keywords:
3D printing bone scaffold
Bio-inspired design
Biomechanics
Computational fluid dynamics
Osteogenesis

ABSTRACT

A porous structure is essential for bone implants because it increases the bone ingrowth space and improves mechanical and biological properties. The biomimetically designed porous Voronoi scaffold can reconstruct the structure and function of cancellous bone; however, its comprehensive properties need to be investigated further. In this study, algorithms based on scaling factors were used to design the Voronoi scaffolds. Classic approaches, such as computer-aided design and the implicit surface method, have been used to design Diamond, Gyroid, and I-WP scaffolds as controls. All scaffolds were prepared by selective laser melting of titanium alloys and three-dimensional printing. Mechanical tests, finite element analysis, and *in vitro* and *in vivo* experiments were performed to investigate the biomechanical, cytologic, and osteogenic performance of the scaffolds, while computational fluid dynamics simulations were used to explore the underlying mechanisms. Diamond scaffolds have a better loading capacity, and the mechanical behaviors and fluid flow of Voronoi scaffolds are similar to those of the human trabecular bone. Cells showed more proliferation and distribution on the Diamond and Voronoi scaffolds and exhibited evident differentiation on Gyroid and Voronoi scaffolds. Bone formation was apparent on the inner part of the Gyroid, the outer part of the I-WP, and the entire Diamond and Voronoi scaffolds. The hydrodynamic properties and stimulus response of cells influenced by the porous structure account for the varied biological performance of the scaffolds. The Voronoi scaffolds with bionic mechanical behavior and an appropriate hydrodynamic response exhibit evident cell growth and osteogenesis, making them preferable for porous structural bone implants.

1. Introduction

Porous scaffolds have been documented as some of the best carriers for the structural and functional reconstruction of bone defects and are under intensive focus in bone tissue engineering [1,2]. In the treatment of bone defects, the immediate and long-term stability of bone scaffolds is associated with their porous structure; however, this requires further exploration [3]. In the design stage, the mechanics of the bone scaffold must be evaluated to ensure that the scaffold does not break after implantation, that is immediate stability of the scaffold must be ensured [4]. By contrast, a porous structure is required to provide sufficient space for cell growth and increase the volume of invasion of the surrounding bone tissues for long-term stability [5,6]. Therefore, porous structures should be carefully studied and designed.

To date, there is little agreement regarding the design of bone scaffolds with excellent comprehensive performanc [7,8]. Computer-aided design (CAD) is a rapid method for drawing scaffolds [9] because several online databases provide effective ways to prepare porous structure models, such as computer-aided systems for tissue scaffolds (CASTS). The three-dimensional (3D) structures in nature, such as beetle and wing scales, favor nutrient influx and maintain mechanical rigidity characteristics [10,11]. Triply periodic minimal surfaces (TPMS) or the

* Corresponding author. Honghui Hospital, Xi'an Jiaotong University, China.
E-mail address: jialiang_li@qq.com (J. Li).

https://doi.org/10.1016/j.mtbio.2023.100934
Received 13 November 2023; Received in revised form 22 December 2023; Accepted 27 December 2023
Available online 28 December 2023

implicit surface method (ISM) is an innovative and alternative approach to designing these 3D scaffolds and classical porous structures, including Gyroid, Schwarz's Diamond, and Schoen's Gyroid [12,13]. However, these porous structures exhibit different mechanical, hydrodynamic, and biological performances [14]. Moreover, these scaffolds are characterized by regular repeated structures that differ from the human skeletal structure.

Human cancellous bone has a unique porous structure pattern with irregular distribution of trabecular thickness and pore size [15,16]. This morphology provides a comprehensive representation of the fluid and solid mechanics, osteogenic response, and bone marrow function. Hence, it was deduced that a biomimetic design could improve the comprehensive properties of bone scaffolds. The design method uses data directly from computed tomography (CT) and bone scans; however, this approach is tedious and has limitations in achieving accurate preparation owing to technical barriers [17].

The Voronoi method is a highly controllable and convenient strategy previously proposed for the biomimetic design of bone scaffolds [18]. Only a few parameters, such as the scaling factor and seed density, are required to control the structure of porous scaffolds. In our previous study, a Voronoi bone scaffold was successfully engineered and fabricated and the effects of pore size on hydrodynamics and osteogenesis were discussed [19]. However, previous studies have only considered the mechanics or biological performance of scaffolds, and there is little empirical evidence that the Voronoi scaffold has an advantage over existing regular repeat scaffolds [20–22]. Therefore, a comprehensive assessment of the Voronoi scaffold in fluid and solid mechanics and its osteogenic response is crucial.

In this study, the Voronoi scaffold and three other classical porous structures were designed and 3D printed (3DP). The present study aimed to employ an integrative approach combining computational fluid dynamics (CFD), finite element analysis (FEA), laboratory experiments, and *in vivo* experiments to investigate the comprehensive properties of the Voronoi scaffold and to reveal the hydrodynamic mechanism underlying the effect of the structure on osteogenesis.

2. Materials and methods

2.1. Design, fabrication, and characterization of bone scaffolds

2.1.1. Design of the diamond, gyroid, I-WP, and voronoi scaffolds

In a previous study, we described the design of a Voronoi scaffold (Fig. 1a); which is an algorithm based on a scaling factor; that is, the basic architecture is constructed by scaling a Voronoi cell [19]. Three types of classical scaffolds were designed (Fig. 1b): Gyroid, Diamond, and I-WP. Detailed descriptions of the three scaffolds have been

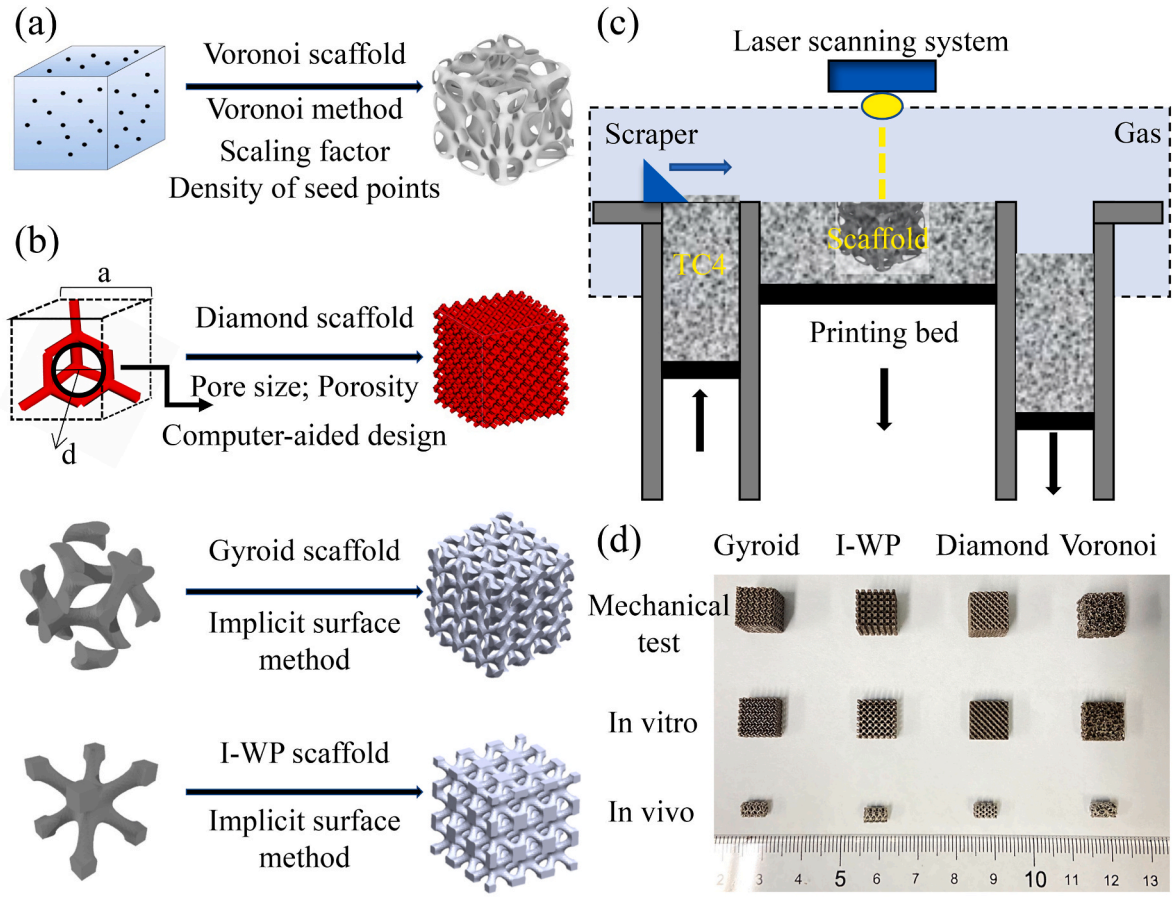

Fig. 1. Design and processing of Diamond, Gyroid, I-WP, and Voronoi scaffolds. (a) The core design of the Voronoi scaffold based on the scaling factor. The model geometric space was established and the seed points were randomly distributed, and then the density of seed points and scaling factor were determined according to the porosity and pore size, and finally the Voronoi method was used to generate the Voronoi scaffold. (b) Design of Diamond, Gyroid, and I-WP scaffolds. Computer-aided design and implicit surface method were used to design a single unit cell of the Diamond, Gyroid, and I-WP, and then expanded to the whole scaffold design. Porosity and pore size are calculated according to the structural characteristics of scaffolds. d is the diameter of the inscribed sphere within the Diamond unit, a is the side length of outer envelope cubic space of the Diamond unit. (c) Selective laser melting (SLM) 3D printing process of titanium alloy (TC4) scaffolds. TC4 powders were spread in a powder bed by a scraper and then laser scanning was carried out layer by layer according to the computer model, and finally any remaining powders were removed to retain the scaffold. (d) Actual scaffolds samples. Cube (side length: 10 mm) for mechanical testing, cuboid (side length: 10 mm and h 5 mm) for *in vitro* studies, and cylinder (φ 4 mm and h 6 mm) for *in vivo* studies.

previously reported, and the related formulas are as follows:

Diamond [23]:

$$D = \frac{3}{2}d \times \cos\alpha - d \tag{1}$$

$$P = \left(1 - \frac{8\pi}{3}\left(\frac{d}{a}\right)^2 + \frac{16\sqrt{2}}{3}\left(\frac{d}{a}\right)^3\right) \times 100\% \tag{2}$$

where D is the pore size, P is the porosity, d is the diameter of the inscribed sphere within the Diamond unit, a is the side length of the outer envelope cubic space of the Diamond unit, and α is 35.5°.

Gyroid [24]:

$$F(x,y,z) = cos(x) * sin(y) + cos(y) * sin(z) + cos(z) * sin(x) - c = 0 \tag{3}$$

I-WP [25]:

$$F(x,y,z) = 2[cos(2\pi x)cos(2\pi y) + cos(2\pi y)cos(2\pi z) + cos(2\pi x)cos(2\pi z)] - [cos(4\pi x) + cos(4\pi y) + cos(4\pi z)] = 0 \tag{4}$$

In this study, the algorithm for designing scaffolds was formulated using Python (Anaconda Inc., USA), and the Voronoi scaffold was designed using the Grasshopper and Rhinoceros3D 7.0 software (Robert McNeel & Assoc). The porosity and pore sizes of all scaffolds were set at 68 % and 800 μm, respectively, based on the previous experiments [19,23]. Three types of scaffolds were designed, including cube (side length: 10 mm) for mechanical testing, cuboid (side length: 10 mm and height: 5 mm) for *in vitro* studies, and cylinder (φ 4 mm and height: 6 mm) for *in vivo* studies.

2.1.2. Selective laser melting (SLM) 3DP of scaffolds

Porous scaffolds were prepared using a Ti–6Al–4V alloy (TC4) and

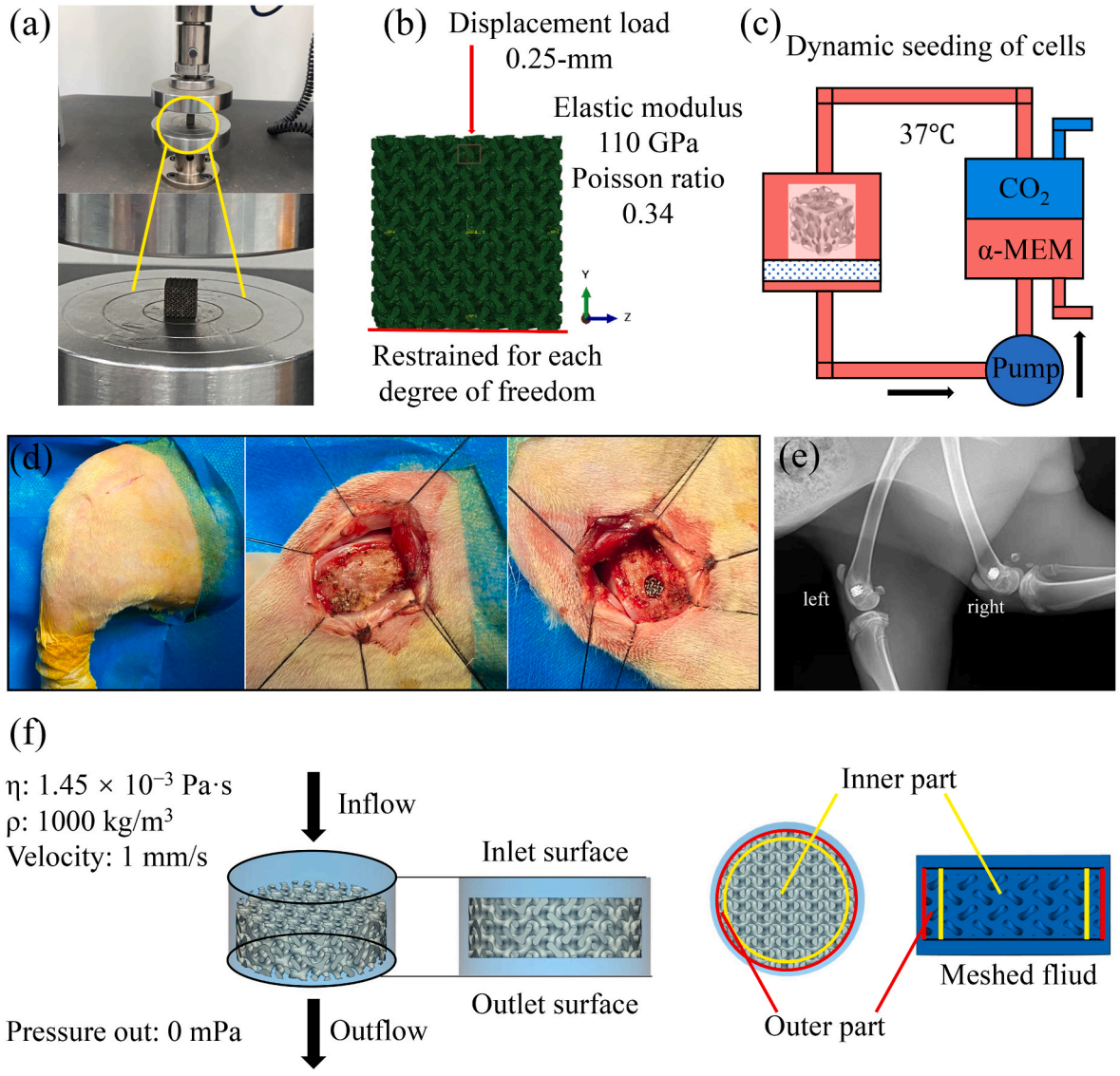

Fig. 2. Diagrams of *mechanical testing finite-element analysis (FEA), cellular and animal experimental methods, and computational fluid dynamics (CFD).* (a) Mechanical testing. (b) FEA; (c) Dynamic seeding of cells. (d) The surgical process of femoral condyle defect modeling of the New Zealand rabbit. (e) Postoperative X-ray detection of scaffolds. (f) CFD simulation. Inlet surface and outlet surface are defined as the surface where the liquid flows through the entire flow field. The scaffold was then divided into an outer part (between the red and yellow lines) and an inner part (between the two yellow lines). (For interpretation of the references to colour in this figure legend, the reader is referred to the Web version of this article.)

manufactured using the SLM 3DP system (BLT-S200, Bright Laser Technologies, China). The processing parameters were as follows: laser power, 225 W; laser scanning speed, 1500 mm/s; powder layer thickness, 0.03 mm; hatching distance, 0.1 mm. After SLM 3DP (Fig. 1c), all the scaffolds were heat-treated at 800 °C for 2 h in an argon gas atmosphere, followed by successive ultrasonic cleaning with ethanol and distilled water.

2.1.3. Micro-CT and scanning electron microscope (SEM) analysis

The morphologies of the four scaffolds were observed using field-emission scanning electron microscopy (SEM; JSM-7900F, JEOL, Japan). All scaffolds were then scanned by micro-CT (YXLON International GmbH, Germany) and reconstructed using the VGStudioMAX 3.0 software (Volume Graphics, Germany) to acquire structural data. The regions of interest (ROI) were set as cubes with a scaffold boundary.

2.1.4. Mechanical testing

The load-bearing capacities of the scaffolds were measured using a mechanical test system (MTS Systems, Inc.). Each scaffold was stressed vertically at a speed of 1 mm/min, and the stress-strain curves were recorded (Fig. 2a).

2.1.5. FEA

The geometric scaffold model was developed in 3-Matic (Materialise, Inc.), meshed in Hypermesh (Altair Engineering, Inc.), and analyzed using ABAQUS (Hib-bitt, Karlsson and Sorenson, Inc.). The Elastic modulus and Poisson's ratio of TC4 were set to 110 GPa and 0.34, respectively. A convergence analysis was conducted to determine the size and number of elements and to ensure that the maximum changes in the strain energy were <3 % (Fig. A1). The mesh element numbers for the scaffolds are listed in Table A1. Periodic boundary conditions were implemented, and a 0.25-mm displacement load was employed in the Z-axis (Fig. 2b). Finally, the yield strength, modulus, and von Mises stress are determined.

2.2. In vitro cell experiments

2.2.1. Dynamic cell seeding and culturing

Pre-osteoblastic MC3T3-E1 cells were provided by the Cell Bank of Typical Culture Preservation Committee of Chinese Academy of Sciences (Shanghai, China). Cells were seeded onto the scaffolds using a previously described dynamic method [19,23] (Fig. 2c), To simulate the *in vivo* environment, 20 mL of the suspension containing 200,000 cells was allowed to penetrate into the scaffold in a single direction, seeded at a speed of 0.5 mm/s, and cultured in α-MEM with 1 % penicillin/streptomycin (P/S) and 10 % fetal bovine serum (FBS; Gibco, USA) at 37 °C and 5 % CO_2. The medium was replaced every 2 days.

2.2.2. Cell absorption

After 24-h of dynamic culture, the cells were fixed with 2.5 % glutaraldehyde (Solarbio Science & Technology, China) at 4 °C for 8 h, followed by dehydration in a gradient of 30–90 % alcohol, and drying in vacuum. After spraying with gold, the morphology of the adherent cells on the scaffolds was observed using low-vacuum SEM (Hitachi, TM3000, Japan). The other scaffolds were removed, washed with phosphate-buffered saline (PBS), fixed in 4 % paraformaldehyde, and treated with 0.5 % triton X-100 at 25 °C. Fluorescein isothiocyanate (FITC)-phalloidin (100 nM) was added to stain the filamentous actin for 30 min, and DAPI (100 nM) was used to stain the nucleus for 30 s in the dark. Finally, the distribution of cells on the scaffolds was visualized using an inverted fluorescence microscope (Olympus, Japan).

Table 1
Parameters of CAD model of scaffolds and reconstruction model by micro-CT.

	Porosity (%)		Specific surface area (mm^{-1})	
	CAD	Micro-CT	CAD	Micro-CT
Gyroid	68.70	67.23	10.08	11.30
I-WP	68.52	69.84	7.29	7.80
Diamond	66.13	64.37	7.77	8.59
Voronoi	69.44	70.87	9.36	9.43

CAD: computer-aided design.

2.2.3. Cell proliferation and differentiation

One to seven days after dynamic seeding, the scaffolds were removed and placed in 24-well plates. A volume of 1000 μL cell counting kit-8 (CCK-8) reagent was added, and the system was then incubated at 37 °C in the dark for 2 h. Subsequently, the absorbance was measured at 450 nm (BioTek, USA) to detect cell proliferation (n = 3).

On day 7 of dynamic culture, the medium was replaced with α-MEM containing 10^{-8} mol/L of dexamethasone, 10 mmol/L of sodium β-glycerophosphate, 50 mg/L of ascorbic acid (Solarbio Science & Technology) to induce cell differentiation. On days 7, 14, and 21 after induction, the levels of alkaline phosphatase (ALP) were detected using an ALP Assay Kit (Beyotime, China), calcium levels were detected using a Calcium Colorimetric Assay Kit (BioVision, USA), and the dsDNA content of the cells on the scaffold was detected using a Quanti-iT dsDNA measurement kit (Invitrogen, USA) for calibration (n = 3). Mature osteoblasts secrete a mineral matrix, which leads to calcium deposition. Extracellular matrix mineralization was detected using a quantitative method [26,27]. The mineralized nodules were solubilized in 10 % hexadecylpyridinium chloride sodium phosphate solution (Solarbio Science & Technology), incubated at room temperature for 10 min, and the absorbance was measured at 562 nm (n = 3).

2.2.4. Quantitative real-time polymerase chain reaction analysis (qRT-PCR)

Osteogenesis-related genes were detected in early (day 10) and late (day 20) cell differentiation stages. Briefly, the cells were lysed to collect the total RNA, and its concentration and purity were determined (Nano Drop 2000, Thermo Fisher Scientific, USA). Reverse transcription was performed using the HiFiScript cDNA Synthesis Kit (Cowin Bio, China), and the primers used are listed in Table A2. The amplification system was prepared according to the instructions of the RT-PCR kit (UltraSYBR Mixture, Cowin Bio). The gene was amplified by forty cycles of PCR reactions. The relative level of the target gene to the housekeeping gene *GAPDH* ($2^{-\Delta\Delta t}$) was calculated for statistical analysis (n = 3).

2.3. In vivo animal experiments

All animal procedures and experiments (including euthanasia) were approved by the Ethics Committee of Xi'an Jiao Tong University and performed in compliance with the regulations of the Administration of Affairs Concerning Experimental Animals of China.

2.3.1. Surgical procedure

Twenty adult male New Zealand rabbits (3–3.5 kg) were obtained from the Animal Experiment Center of Xi'an Jiao Tong University and randomly divided into two groups (implantation times of 6 and 12 weeks). In each group, 20 femurs from 10 rabbits were randomly assigned to one of four types of scaffolds (n = 5). Based on weight, 3 mg/kg propofol (Petsun, China) was used to induce anesthesia, and 1.5 % isoflurane (Bucolic, China) was administered to maintain anesthesia. An animal-specific ventilator (Mindray, Shanghai, China) was used to

Table 2
Yield Stress (MPa) of scaffolds analyzed in MTS and FEA.

	Gyroid	I-WP	Diamond	Voronoi
MTS	48.63	70.80	104.77	81.58
FEA	48	65	110	83

MTS: mechanical test system; FEA: finite element analysis.

maintain normal ventilation. After aseptic sterilization, a 3-cm incision was made on the medial skin of the femoral condyle, the scaffold was implanted after drilling the bone defect area, and finally, the surgical incisions were sutured in layers (Fig. 2d). Postoperative X-ray (Fig. 2e) was used to observe the positions of the scaffolds. After surgery, cefazolin was intramuscularly injected at a dose of 10 mg/kg once daily. Femoral samples were collected after the animals were euthanized (at 6 and 12 weeks) and fixed in 4 % paraformaldehyde for subsequent studies.

2.3.2. Micro-CT analysis

Micro-CT was used to observe osteogenesis and quantitatively analyze newly formed (NF) bone. The ROI consisted of two parts: the surrounding ROI (the area within 1 mm of the scaffold) and the overall ROI (the 3D space occupied by the scaffold), which was further divided into inner and outer ROI according to half of the diameter. BV/TV is the ratio of bone volume to space volume, which reflects the amount of NF bone.

2.3.3. Fluorescent labeling of the NF bone

Calcein (10 mg/kg; Sigma, USA) and alizarin complexone (30 mg/kg; Sigma) were injected at the 4th (early-stage) and 8th (late-stage) weeks after the operation, respectively, to evaluate the NF bone at different time points. After the femoral condyle was harvested, the hard tissue sectioning system was used to cut the samples into approximately 50-μm sections along the long axis of the scaffold (Leica SP 1600, Germany). The sections were observed under an inverted fluorescence microscope (Olympus).

2.3.4. Histological evaluation

The sections were stained with VG staining (1.2 % trinitrophenol and 1 % acid fuchsin) and Goldner (Weigert iron hematoxylin, Acid Ponceau, Orange G, and Bright green dye) and observed under an optical microscope (Olympus).

2.4. CFD simulation

The scaffold and fluid domain models were established using the 3-Matic software, meshed in the Hypermesh software, and calculated using the Fluent 6.3 software (Ansys) (Fig. 2f). The porous scaffold was located in the middle of the fluid domain model and was defined as an impermeable and rigid region, and a no-slip surface condition was assumed. The spacing between the flow field and the scaffold model was set to 0.5 mm to simulate the liquid environment of dynamic perfusion culture in cell experiments. The fluid properties were set as α-MEM at 37 °C with a viscosity (η) of 1.45×10^{-3} Pa s and density (ρ) of 1000 kg/m^3. An inlet velocity of 1 mm/s was applied to the scaffold. The fluid was set to a laminar flow because the Reynolds number was <10 [28], and the outlet surface was set at zero pressure. Finally, the permeability (k), mass flow, flow rate, and wall shear stress (WSS) were extracted and calculated after the simulation. The permeability (k) of the scaffold was calculated using the Wang–Tarbell formula [29], mentioned in Eq. (5).

$$K = \left(\frac{\eta v}{\tau}\right)^2 \tag{5}$$

where η is the fluid viscosity, v is the flow velocity, and τ is the mean WSS on the scaffold.

2.5. Statistical analysis

The data were expressed as mean ± standard deviation and analyzed using SPSS (version 19.0, SPSS Inc., USA). A repeated-measures analysis of variance (Brown–Forsythe and Welch ANOVA tests) with Tukey's post-hoc test was applied to compare the four groups. *P*-values <0.05 were considered statistically significant.

3. Results

3.1. Characteristics of porous scaffolds

Scaffolds with specific shapes were successfully prepared using SLM 3DP (Fig. 1d). SEM observations (Fig. 3a) showed that the scaffold morphology was consistent with that of the CAD model. No breakage of the trabeculae was observed, and the TC4 particles on the scaffold surface were tightly bound, creating a complex, irregular nanostructure. The parameters of the micro-CT and CAD models were similar (**Table 1**), and no blockage of the micropores was detected in the micro-CT scan (Fig. 3b).

3.2. Mechanical properties of the scaffolds

As shown in Table 2, the order of the yield stress of the scaffolds from high to low was Diamond, Voronoi, I-WP, and Gyroid, consistent with the findings of the FEA and MTS tests (Fig. 3c). FEA is shown in Fig. 4. On the Gyroid scaffold, stress was transferred along a uniform distribution on the surface of the undulating trabecular. Stress concentration occurs at the splicing junction of single units in the I-WP and Diamond scaffolds, and the I-WP scaffold has low mechanical strength because of the lack of structural support. On the Voronoi scaffold, the stress was mainly conducted on the vertical stout trabecular and was not distinct in the thin and small trabecular, which is analogous to the load-carrying mechanism of the trabecular bone—the thick bone tissue is the main force of weight-bearing.

3.3. Cell adhesion and distribution

As shown in Fig. 5a, the cellular distribution throughout the scaffolds was visualized using fluorescent staining (FITC-phalloidin and DAPI). Many cells were attached to the undulating trabecular in the Gyroid scaffold and to the platform structure in the I-WP scaffold. However, almost no fluorescent signal was observed in the interior of the I-WP scaffold, indicating the absence of cells. Cell distribution was also conspicuous along the rods of the Diamond scaffold and was markedly pronounced on the irregular trabeculae of the Voronoi scaffold. SEM observations revealed that the cells grew and spread adequately on the surface of the scaffold, and their pseudopods were connected to the surrounding particles, indicating satisfactory biocompatibility of TC4 (Fig. 5b) and (Fig. A2).

3.4. Cell proliferation and differentiation

The proliferation of cells on all the scaffolds increased in a time-dependent manner (Fig. 5c), and that on the Voronoi scaffolds was significantly higher than that on the other scaffolds ($P < 0.05$). The ALP and calcium ion levels of cells on the Voronoi scaffolds peaked 14 days after osteogenic induction and were significantly higher than those on the I-WP scaffolds ($P < 0.05$) (Fig. 5d). The order of the degree of mineralization from high to low was as follows: Voronoi, Gyroid, and Diamond, and I-WP scaffolds ($P < 0.05$), suggesting that the osteogenic activity of the cells on the surface of the Voronoi scaffold was significant. The expression levels of osteogenesis-related genes on the different scaffolds were detected using qRT-PCR (Fig. 5e). In both the early (10 days) and late (20 days) osteogenic activities, the *BMP-2, ALP, OPN, and OCN* genes were highly expressed on the Voronoi scaffolds ($P < 0.05$). Moreover, the Diamond scaffolds increased *Runx-2* expression ($P < 0.05$), but no significant difference was detected in the *Col1α1 gene* expression between the groups in the late stage.

3.5. Micro-CT analysis

As shown in Fig. 6a, the surrounding ROI reflected a bidirectional influence on the scaffolds and pre-existing bone tissues, indicating that

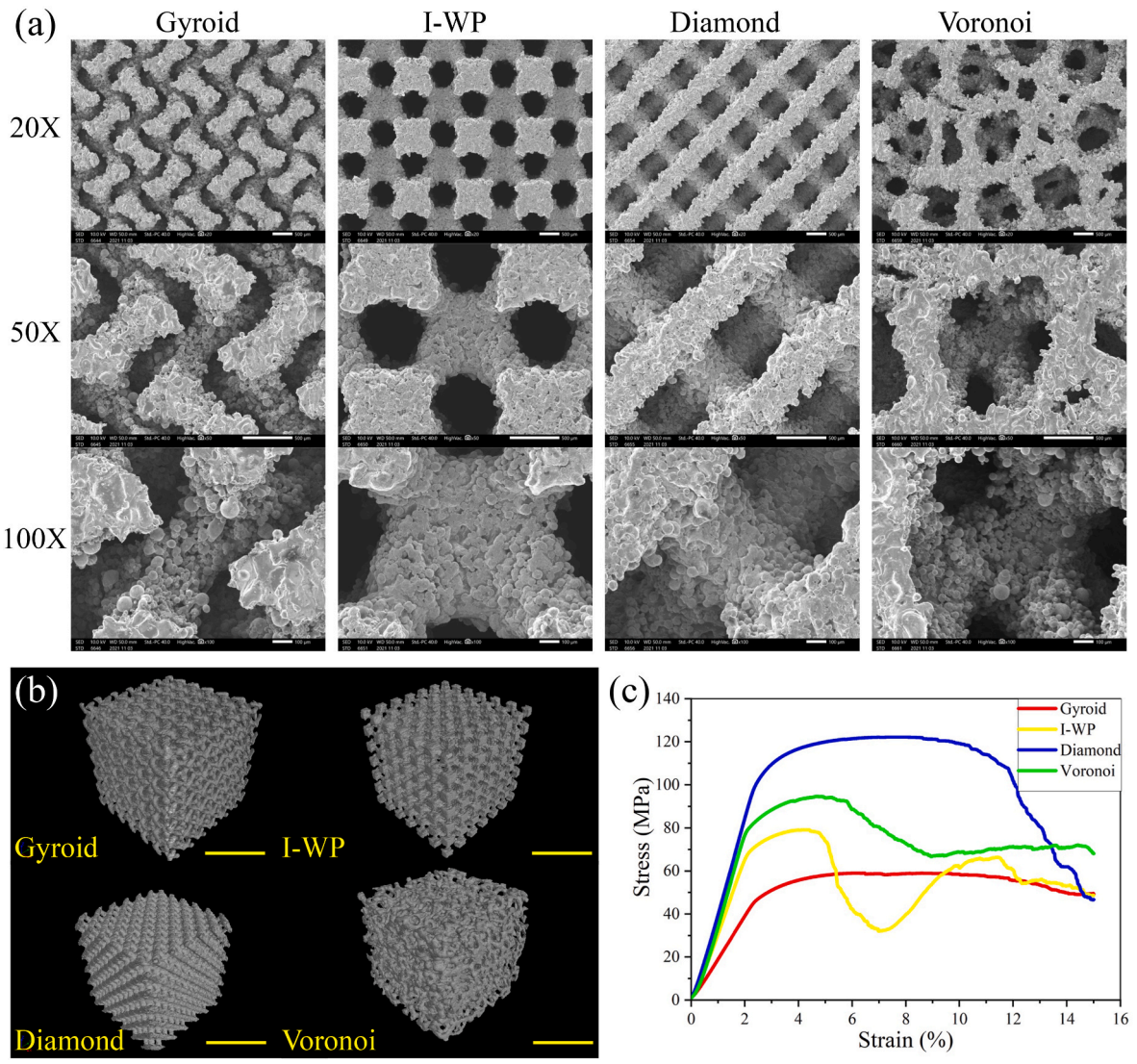

Fig. 3. *Characteristic and mechanical test of scaffolds.* (a) scanning electron microscope images of surface characteristics of scaffolds. The scalebar of the 20X and 50X is 500 μm; the scalebar of the 100X is 100 μm. (b) Reconstruction model of scaffolds by micro-CT scanning. Scalebar: 5 mm. (c) The stress-strain curves.

the Voronoi scaffold was sufficiently wrapped by the surrounding bone. For the whole scaffold, in the early postoperative period (6 weeks), NF bone was formed on the external surface of the scaffolds, and bone formation increased with the implantation time in each scaffold. In the late period (12 weeks), the NF bone in the Voronoi scaffold was significantly greater than that in the Gyroid and I-WP scaffolds, which was consistent with the results of the quantitative micro-CT analysis ($P < 0.05$) (Fig. 6b). The overall ROI was artificially divided into inner and outer parts further to describe the bone ingrowth quality of the scaffold (Fig. 6c). A large amount of NF-bone was observed in the inner part and much less in the outer part, which was more evident in the Gyroid scaffolds, whereas the Diamond and I-WP scaffolds showed greater bone regeneration in the outer part. The NF bone was adequately distributed on the entire Voronoi scaffold and covered almost all fields. Quantitative analysis showed that the Voronoi scaffold exhibited the highest BV/TV ($P < 0.05$) (Fig. 6d).

3.6. Fluorescent markers of NF bone

The NF bone was labelled to reflect the osteoplastic activity on the surface of the scaffold at the early (green) and late (red) stages. Fig. 7a shows the green early NF bone immediately adjacent to the TC4 surface of the scaffolds and the red late NF bone extending from the early NF bone. NF bone in the inner and outer pore spaces was visualized in all scaffolds, and early NF bone on the surface was pronounced in the Voronoi scaffolds.

3.7. VG and goldner staining

VG staining showed that the NF bone was visible on the exterior side of each scaffold after 6 weeks. At 12 weeks (Fig. 7b), the NF bone was more prominent on the outer layer of the I-WP scaffolds, whereas the new bone formation on the Gyroid, Diamond, and Voronoi scaffolds was evident throughout the entire region. Additionally, a successful osseous bridging connection was observed in the pore area inside the Voronoi scaffold (yellow circle in Fig. 7b). Goldner staining could differentiate between mineralized bone and osteoids (Fig. 7c). Mineralization was observed in the area surrounding each scaffold and was evident in the inner part of the Gyroid scaffold. In contrast, more osteoid bone tissue was detected in the interior of the I-WP scaffold than in mature mineralized bone.

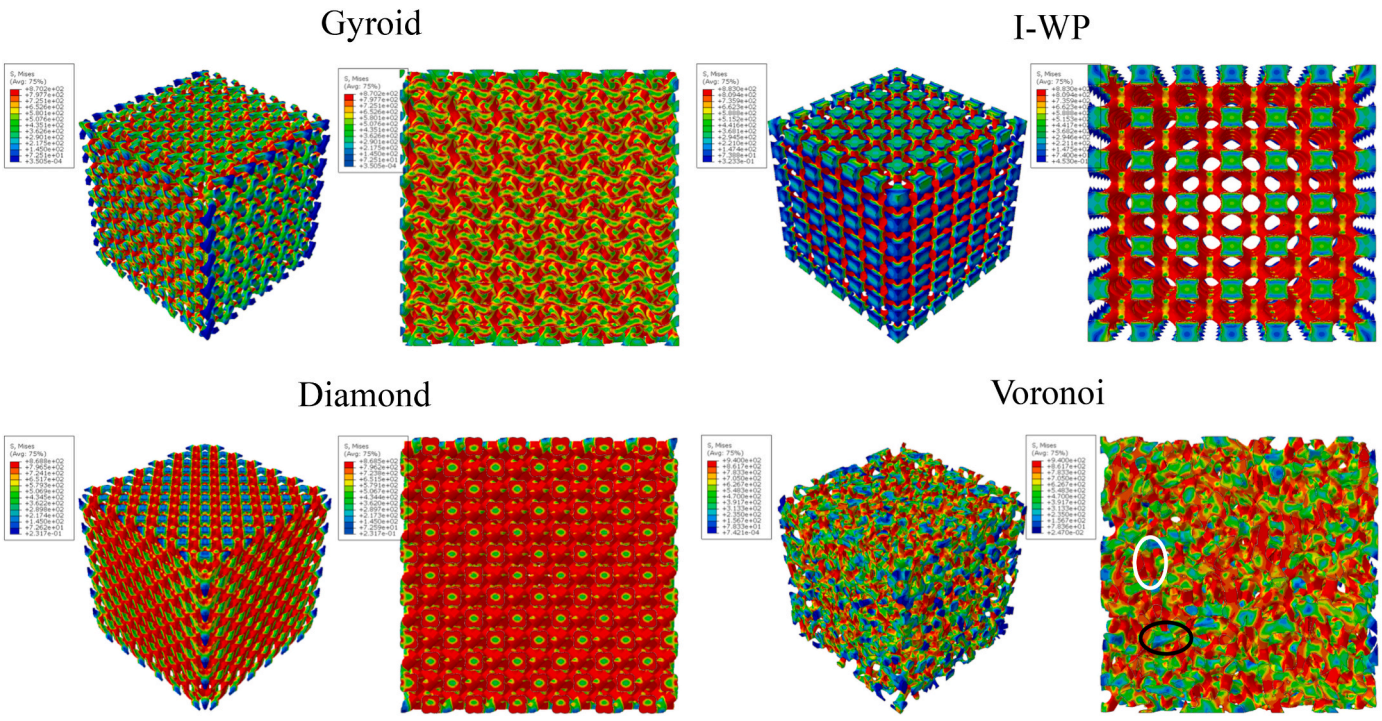

Fig. 4. *FEA. Stress distribution in each scaffold.* The vertical stout trabecular is denoted by white circles, and the nearly horizontal and thin trabecular is denoted by black circles, in the Voronoi scaffold.

3.8. Flow rate and permeability

α-MEM flowing through the scaffold post-CFD simulation is illustrated in Fig. 8a. When the liquid flowed through the Gyroid scaffolds, there was more fluid outside and less fluid inside the scaffolds. However, the I-WP scaffold demonstrated the opposite performance; that is, more liquid flowed through the scaffold. For the Diamond scaffold, the fluidic distribution of the flow was uniform, and the average flow rate through the scaffolds was the highest (Fig. 8b). According to Eq. (5), the permeability K of scaffolds ranking from high to low was I-WP ($85.7 \times 10^{-10}mm^2$), Diamond ($66.2 \times 10^{-10}mm^2$), Voronoi ($41.5 \times 10^{-10}mm^2$), and Gyroid ($33.2 \times 10^{-10}mm^2$) scaffolds.

3.9. Distribution of WSS

In terms of the overall scaffold, the WSS responses were 24.1 mPa (Gyroid) > 20.0 mPa (Diamond) > 18.2 mPa (Voronoi) > 15.7 mPa (I-WP), respectively, with significant differences ($P < 0.01$) (Fig. 8c). To alleviate the influence of the region on WSS, the scaffolds were divided into inner and outer parts for analysis. Moreover, the WSS responses outside and inside the scaffolds were consistent with those of the overall scaffold (Fig. 8de). The frequency distribution of the element WSS represents the area ratio of the WSS distribution. The distribution peaks of the outer WSS of the Gyroid, I-WP, and Diamond scaffolds were at 25–30 mPa and were more significant than those of the Voronoi scaffold (5–10 mPa). However, the areas >35 mPa of the inner Voronoi scaffolds were larger than those of the other three scaffolds.

4. Discussion

The immediate stability of bone implants, which prevents the surrounding bone from collapsing and causing implant destruction, is a major concern. Therefore, filled implants with strong loading capacities have been widely used [30]. However, osseointegration only occurs at the outer surface, and there is no possibility of bone ingrowth in the filled implants because of insufficient space, which may cause fusion failure between the implants and bone [31]. The reconstruction of the 3D structure and function of the trabecular bone is the core of bone repair, in which a porous scaffold is a research priority [32,33].

In previous studies, the fundamental structural characteristics of the scaffold were often regular geometries based on the ISM or CAD method [34], which mainly focused on the mechanical behavior of the porous scaffolds. However, the structure of human bone, showing irregular trabecular morphology and non-uniform pore size distribution, exhibits the highest performance in fluid and solid mechanics and osteogenesis [35,36]. Although representative, bionic bone designed based on CT data may not be valid for other implantation sites because of variability in the characteristics and structure of the bone [37]. A parametric design method based on the Voronoi structure is an efficient and controlled approach for simulating cancellous bone [38]. Thus, biomechanical and biological experiments show that the porous structure can be modified to adapt to implantation requirements. In a previous study, we observed that the Voronoi scaffold with a designed pore size of 800 μm and a pore size distribution of 458.8–989.1 μm is optimal for trabecular scaffolds [19]. It is worth noting that the pore size, porosity, and rod diameter affect the performance of the scaffold, with pore size being a key factor in bone regeneration. Therefore, the pore size of all scaffolds in this study was set to 800 μm. Nevertheless, a comprehensive assessment of the Voronoi scaffold is insufficient compared with that of other bone scaffolds.

Considering the effect of the material on osseointegration, TC4, which has biocompatibility and extensive applications, was used to fabricate bone scaffolds in this study [39]. All scaffolds were successfully prepared using SLM 3DP and exhibited different structural features. The trabecular and pore structure of the Gyroid scaffold is continuous and wavy; the platform in the I-WP scaffold consists of solid arcs of adjacent single unit, in which the voids form vertical channels, small rods of the Diamond units are interwoven into a porous meshwork, and the trabecular with inhomogeneous structures interlace each other and form irregular pores with different shapes and sizes in the Voronoi scaffold. Micro-CT reconstruction analysis revealed the porous features of the four types of scaffolds. Notably, the differences between these intricate

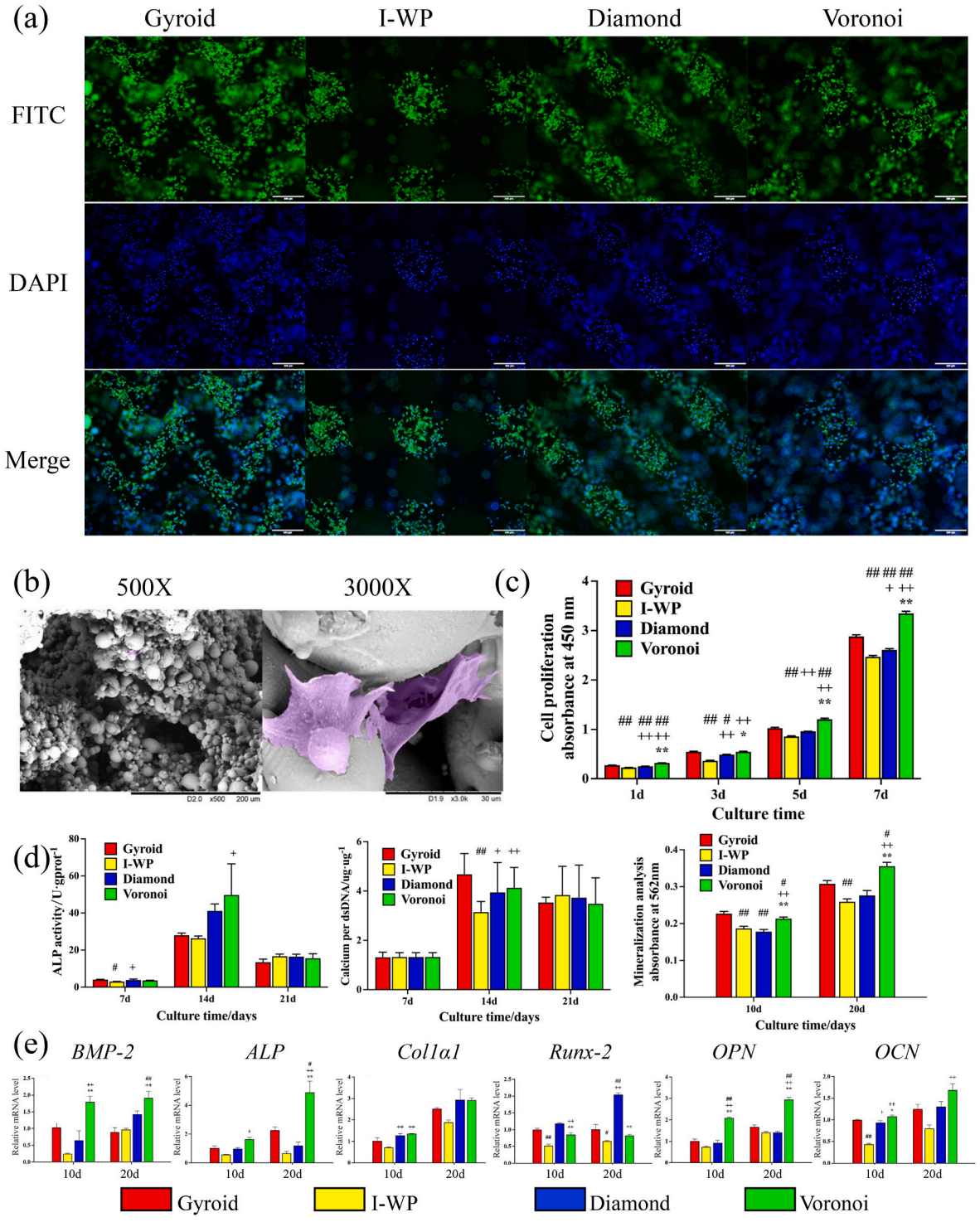

Fig. 5. *Cell adhesion, distribution, proliferation and differentiation.* (a) Distribution of MC3T3 cells on scaffolds. Green: filamentous actin stain by fluorescein isothiocyanate (FITC)-phalloidin; Blue: the nucleus stain by DAPI; Scalebar: 500 μm. (b) SEM of cell adhesion on the Voronoi scaffold. The scalebar of the 500X is 200 μm; the scalebar of the 3000X is 20 μm. (c) Quantitative analysis of cell proliferation. (d) Detection of alkaline phosphatase (ALP) and calcium ion level, and mineralization. (e) qRT-PCR detection of osteogenesis-related genes. $P(\#) < 0.05$ and $P(\#\#) < 0.01$ compared with Gyroid scaffold; $P(+) < 0.05$ and $P(++) < 0.01$ compared with I-WP scaffold; $P(*) < 0.05$ and $P(**) < 0.01$ compared with Diamond scaffold. (For interpretation of the references to colour in this figure legend, the reader is referred to the Web version of this article.)

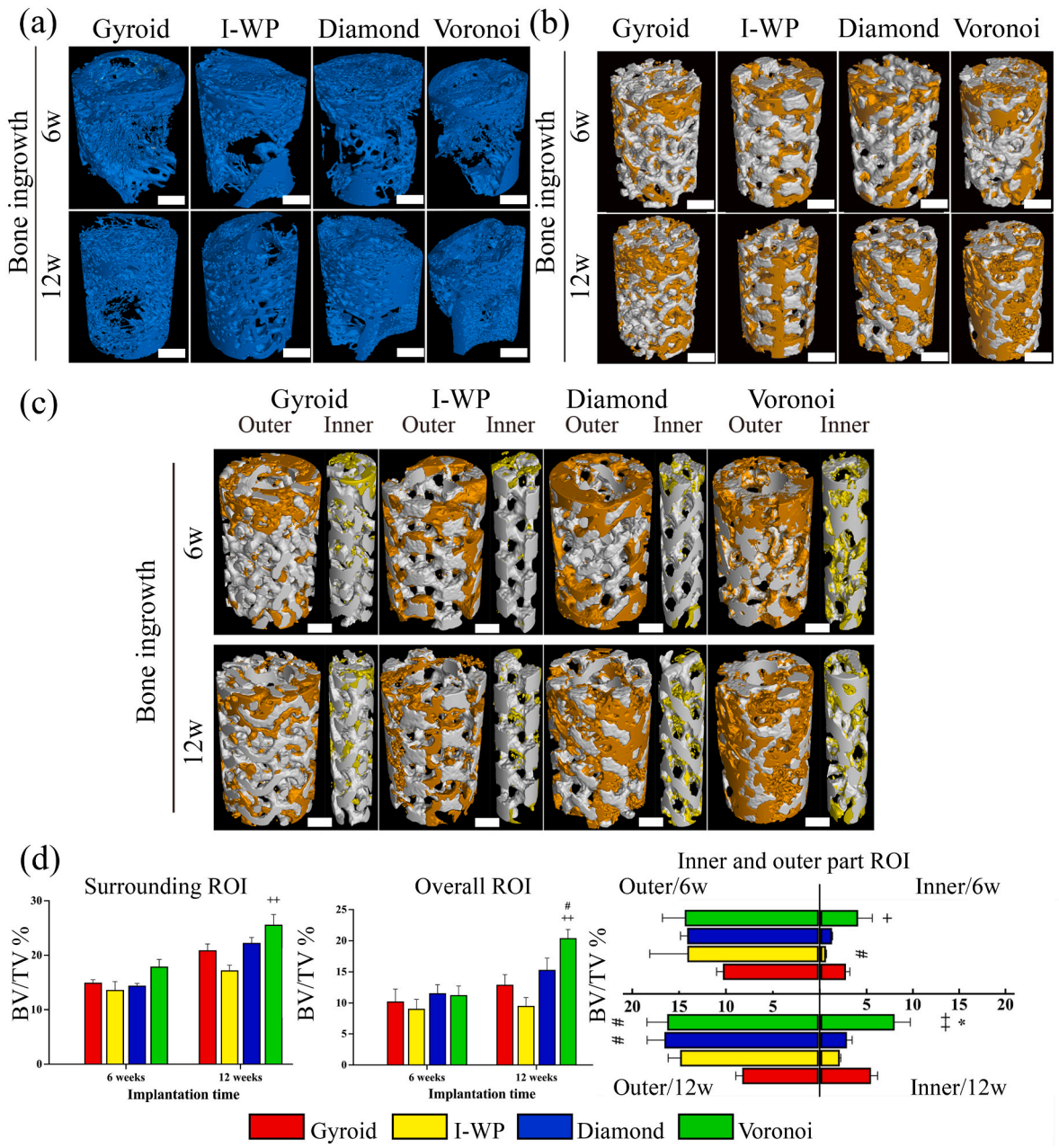

Fig. 6. Osteogenesis on scaffolds analysis by Micro-CT. (a) The surrounding bone tissues. Scalebar: 1 mm. (b) The overall osteogenesis of the scaffold. Scalebar: 1 mm. (c) The inner and outer osteogenesis of the scaffold. Scalebar: 1 mm. (d) The surrounding BV/TV, overall BV/TV, inner and outer part BV/TV of the scaffold. *P (#) < 0.05* compared with Gyroid scaffold; *P(+) < 0.05* and *P(++) < 0.01* compared with I-WP scaffold; *P(*) < 0.05* compared with Diamond scaffold.

3D porous structures would lead to differences in their biomechanical and biological performances.

The loading capacity of a scaffold is crucial for bone implants to restore the stability of the implantation area. Based on mechanical testing, FEA can explain force transmission and stress distribution meticulously and intuitively. The Gyroid scaffold had the lowest yield strength because its wavy trabeculae lacked a vertical support structure and was finer under the same porosity. Although the rod diameter of the I-WP scaffold was greater than that of the Gyroid scaffold, an obvious stress concentration at the splicing junction and lack of structural support led to insufficient load-bearing capacity. Under optimal stress, the scaffold formed by the diamond cubic lattice structure shows a marked effect on the mechanical properties because of the force decomposition. This is one of the reasons for the extensive use of the diamond structure in bone implants [40,41]. Under compression loading conditions, the vertical stout trabecular of the Voronoi scaffold plays a major role in force conduction and transmission, which is consistent with the physiological load-bearing behavior of the human skeleton [42]. The trabecular bone is thickened, and the skeletal mass is increased to adapt to the high mechanical stress stimulation, as loading insufficiency results in osteopenia or osteoporosis [43,44]. Some studies have also reported that an irregular structure enhances the mechanical strength of bio-inspired scaffolds [45].

The biological performance of scaffolds is influenced by the behavior of cells on the scaffolds, including cell adhesion, distribution, and proliferation [46]. SEM observations revealed a large number of TC4 particles on the surfaces of all scaffolds, which increased the cell contact area and led to cell expansion (Fig. A2). The results of the CCK8 test demonstrates the sustained growth of cells on the surface of the scaffold. Therefore, we can infer that the cells adhered well to all the scaffolds

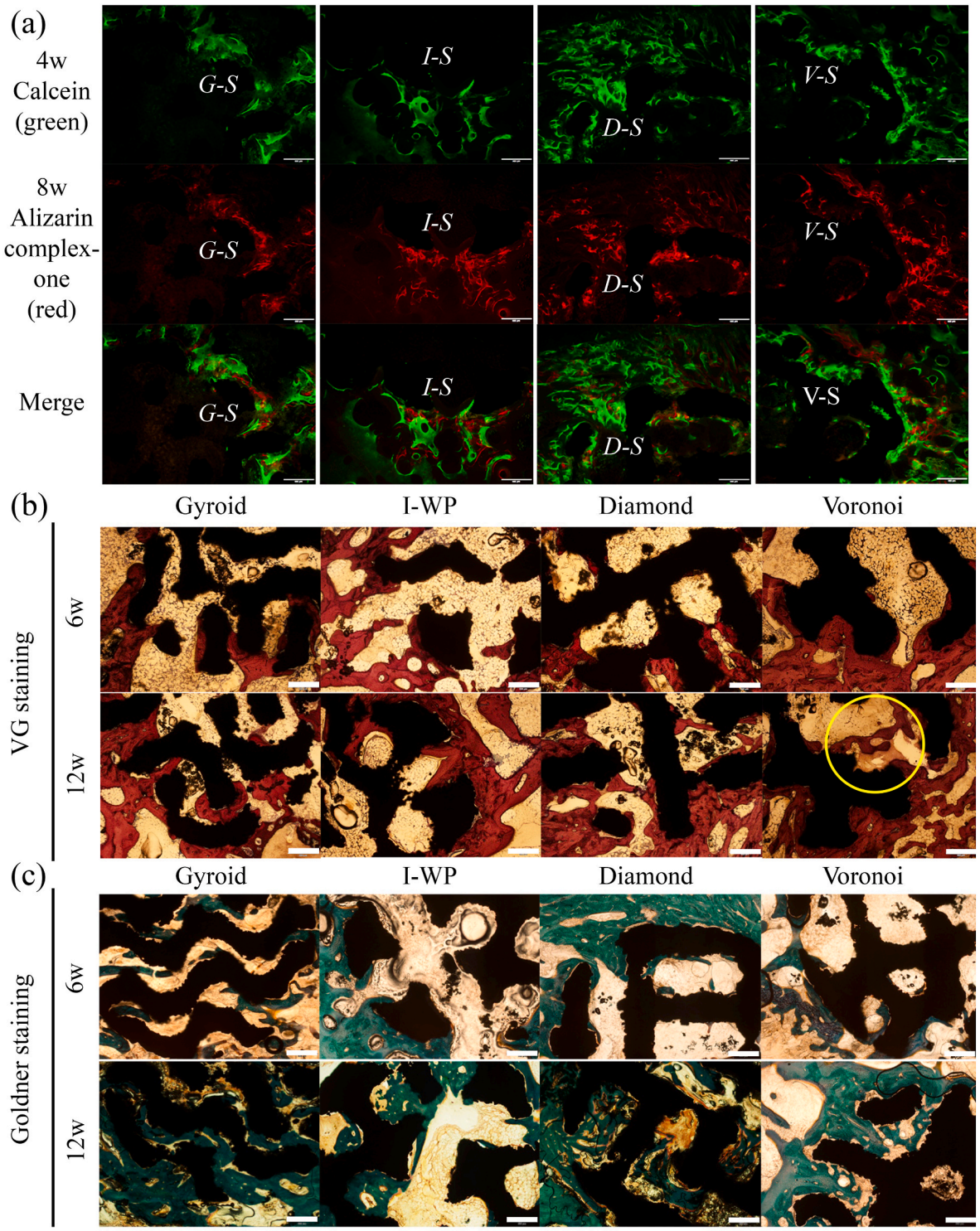

Fig. 7. Fluorescent markers of newly formed bone and tissue staining for osteogenic analysis. (a) Observation by inverted fluorescence microscope. Calcein (green labels) and Alizarin complexone (red labels) was injected in the 4th and 8th week after the operation, respectively. G–S: Gyrooid scaffold; I–S: I-WP scaffold; D–S: Diamond scaffold; V–S: Voronoi scaffold. Scalebar: 500 μm. (b) The observation of VG staining at 6 and 12 weeks after the operation, respectively. Bone: red; Scaffold: black; Cell nucleus: blue. Scalebar: 500 μm. Yellow circle: microporous interior osteogenesis and osseous bridging connection. (c) The observation of Goldner staining at 6 and 12 weeks after the operation, respectively. Mineralized bone: blue-green; Scaffold: black; Osteoid: orange. Scalebar: 500 μm. (For interpretation of the references to colour in this figure legend, the reader is referred to the Web version of this article.)

based on both qualitative and quantitative observations. Because the pore size is much greater than that of the cell, the porous scaffold mainly affects cell distribution rather than adhesion which is primarily associated with material characteristics [47]. The morphology and structure of the scaffolds were the main factors affecting cell distribution, and MC3T3 cells were mainly distributed in the perpendicular plane facing the liquid inflow. The horizontal trabecular or rods in the Gyroid, Diamond, and Voronoi scaffolds originally acted as a barrier structure for flows, but became the cell distribution area. In contrast, only a small number of cells were observed in the I-WP scaffold platform structure.

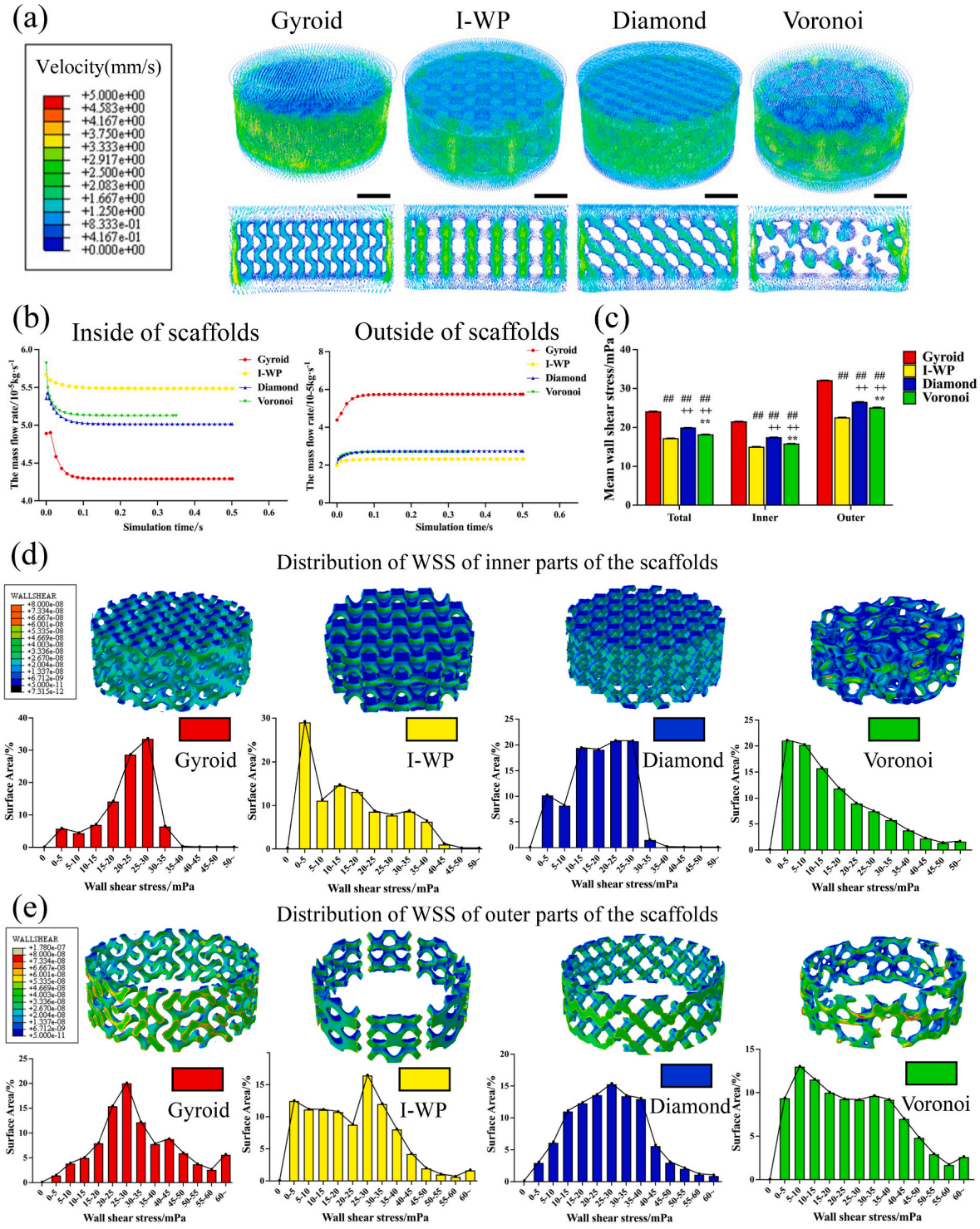

Fig. 8. Computational fluid dynamics analysis. (a) Visual images of fluid passing through the scaffolds. The direction of the streamline represents the direction of liquid flow, the color of the streamline represents the flow velocity, and the density of the streamline represents the flow rate. The higher the density, the greater the flow rate. Scalebar: 2 mm. (b) The flow of the outside and inside scaffolds. (c) Average wall shear stress (WSS) of the scaffolds. (d, e) Visualized distribution images of WSS of inner and outer parts of the scaffolds. $P(\#) < 0.05$ and $P(\#\#) < 0.01$ compared with Gyroid scaffold; $P(+) < 0.05$ and $P(++) < 0.01$ compared with I-WP scaffold; $P(*) < 0.05$ and $P(**) < 0.01$ compared with Diamond scaffold. (For interpretation of the references to colour in this figure legend, the reader is referred to the Web version of this article.)

The proliferation of the cells on the scaffold increased in a time-dependent manner and was related to the initial cell distribution and nutrient supply. The Voronoi scaffold exhibited markedly improved cell proliferation and even greater cell distribution, which are fundamental to its biological performance. In addition to morphological factors, the parameters of the porous scaffold also affect its cytological behavior. In addition, the irregular pore sizes of the Voronoi scaffolds significantly and positively affected cellular growth and proliferation.

During osteogenic induction, ALP and calcium ions of cells, which are markers of cell differentiation, exhibit high activity and content in the Gyroid and Voronoi scaffolds, indicating that osteogenic differentiation of MC3T3 cells on this scaffold starts early. The extracellular matrix maturation and mineralization are the bases of bone formation and are evident on Gyroid and Voronoi scaffolds. The qRT-PCR assays showed a similar result; the cells on the Voronoi scaffold had a high level of expression of osteogenesis-related genes. This phenomenon may be attributed to the significant cell accumulation and appropriate stimuli to the cells on the Gyroid and Voronoi scaffolds. The differentiation of precursor cells into mature osteoblasts is primarily associated with mechanical stimulation [48]. Thus, it can be speculated that the solid and fluid mechanical properties of the Voronoi scaffold exert beneficial effects on osteogenesis [49].

The effects of the hydrodynamic response and surrounding tissue on the osteogenesis and bone ingrowth of scaffolds can be carefully analyzed *in vivo*. Micro-CT analysis revealed that bone formation began at the outer surface of all the scaffolds and progressively moved inward. However, bone ingrowth and mass details differed significantly among the scaffolds. In the Gyroid scaffold, the NF bone was first formed at each end of the scaffold, and bone ingrowth was obvious in the inner part but insufficient in the outer part, whereas more NF bone was observed in the outer part of the I-WP scaffold in the early stage. NF bone was uniformly formed in the Diamond and Voronoi scaffolds, and the pores of the Voronoi scaffold were adequately filled. Quantitative analysis also demonstrated that the Gyroid scaffold had a high bone volume in the inner part, and that the amount of NF bone was evident in the Voronoi scaffold. Overall, the NF bone was apparent on the inner part of the Gyroid scaffold, outer part of the I-WP scaffold, and entire Diamond and Voronoi scaffolds. The native bone surrounding the surgical area, as a foundation for bone ingrowth and extension [50], is affected by the material and structure of the scaffolds. In this study, all scaffolds were enveloped, at least partially, by bone tissue because of the biocompatibility of TC4. In addition, the Voronoi scaffold showed the greatest accumulation of surrounding bone, providing an opportunity for early bone growth.

Fluorescent markers of the NF bone revealed red late NF bone formation and extension from green early NF bone, confirming the biocompatibility of TC4. Additionally, early NF bone formation was observed on the Voronoi scaffold. VG and Goldner staining showed delineation of the osseous structures, and mineralized bone and osteoids could be distinctly recognized. In addition, the NF bone tissue attaches to the trabecular, accumulates and mineralizes in the scaffold's pores at different positions, which is consistent with the micro-CT features. Moreover, mineralized bone tissue builds bridges between the pore areas inside the Voronoi scaffold, indicating that the structure of Voronoi scaffolds is beneficial for bone remodeling [51].

After bone injury, the blood or bone marrow carrying nutrients and stem cells enter the scaffold and perform physiological functions [52]. Therefore, in addition to their biomechanical properties, the hydrodynamic characteristics of scaffolds are critical to their biological performance [53]. The biological properties of the scaffolds can be explained based on the hydrodynamic performance and stimulus response analyzed by CFD simulations. The morphology of scaffolds affects cell distribution, which in turn affects the site of osteogenesis. Few NF bones were observed in the inner part of the I-WP scaffold owing to the absence of cell adhesion. While a high flow rate and permeability favor the excretion of excreting waste products, they might cause insufficient contact time between the nutrients and cells, which eventually leads to a lower amount of NF bone in the outer Gyroid scaffold and inner I-WP scaffold. Although the Diamond scaffold had strong penetration, sufficient and even cell distribution accounted for uniform osteogenesis. The characteristics of the Voronoi scaffolds and the concurrence of both small and large irregular pores were consistent with those of human cancellous bone. Strikingly, fluids can be rapidly drawn into the macropores in this irregular structure and slowly and gently flow through the small lumens, resulting in adequate cell attachment, good metabolic stability, and thus outstanding osteogenesis performance. In addition to the fluid flow pattern, hydrodynamic stimulation affects cell differentiation [54,55]. A previous study revealed that high-stress stimulation promotes the differentiation of osteoblasts into osteocytes. High WSS zones were observed in the inner Gyroid scaffold and outer I-WP scaffold, and the distribution of WSS in the Diamond and Voronoi scaffolds became homogeneous, which could be ascribed to the varied osteogenic performances of the scaffolds.

Taken together, the biomechanical and hydrodynamic characteristics of the Voronoi scaffold account for its outstanding biological performance. However, this study had some limitations. Although the pore size and porosity of all scaffolds were consistent, the differences in rod diameters owing to different basic structures may have an impact on the biological performance. As the pore size of the scaffold is a key factor in bone regeneration and was set to be consistent in this study, we believe that the influence of pore size on bone regeneration was alleviated. There remains a gap between the symmetric boundary condition in the CFD analysis and the actual bone circulation environment because the fluid direction inside the skeleton is diverse. Therefore, based on the advancements in computer and manufacturing technologies, biomimetic scaffolds based on Voronoi structures must be investigated further. In addition, the TC4 used in this study exhibited a high elastic modulus, which might cause stress shielding [56], thus leading to bone resorption. Hence, scaffolds materials are worthy of further exploration.

5. Conclusions

In this study, the Voronoi, Gyroid, I-WP, and Diamond scaffolds were successfully designed and prepared from TC4 and 3DP using SLM. FEA and *in vitro* and *in vivo* experiments were used to explore the effect of structure and morphology on the biomechanical properties and osteogenesis of the scaffolds, while CFD was used to analyze the underlying hydrodynamic mechanism. The following conclusions were derived.

(1) The structures and morphologies characterizing the Voronoi structural scaffold exhibit similarities to those found in human cancellous bone.
(2) The Diamond and Voronoi scaffolds had better load-bearing capacity than other scaffolds, and the mechanical behavior of the Voronoi scaffold was consistent with that of the human skeleton.
(3) Cell distribution, proliferation, and osteogenic differentiation were apparent in the Voronoi scaffold compared to those in other scaffolds.
(4) New bone formation was more apparent on the inner part of the Gyroid scaffold, the outer part of the I-WP scaffold, and entire Diamond and Voronoi scaffolds.
(5) The outstanding biomechanical and hydrodynamic characteristics are potential reasons for an enhanced biological performance of Voronoi scaffold.

Funding

This work was supported by the National Key Research and Development Project of the People's Republic of China (No.2018YFE0114200) and the National Natural Science Foundation of China (No.82072432).

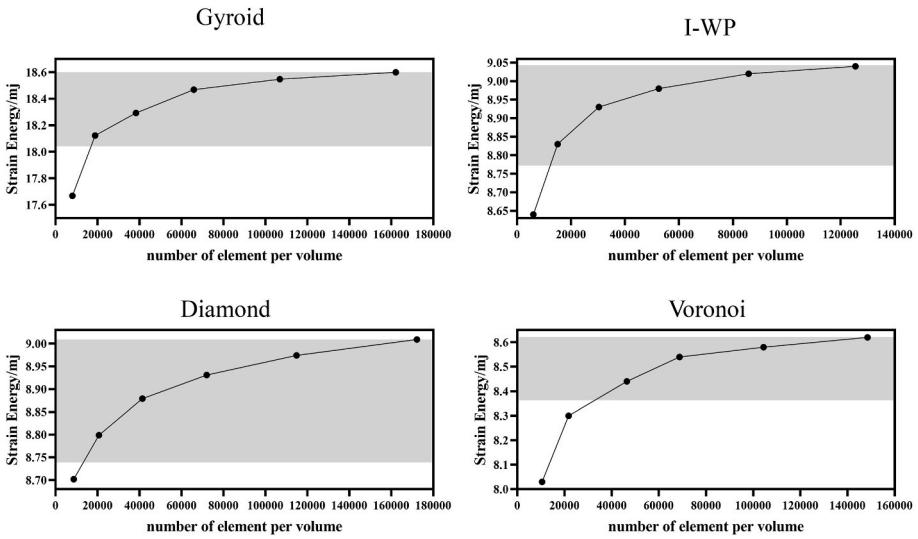

Fig. Appendices 1. A convergence analysis in finite-element analysis. Shaded areas indicate an error of less than 3 %. In the subsequent simulation, the reliability of the simulation data can be guaranteed by ensuring that the mesh density of the finite element model of each scaffold is in the shaded area.

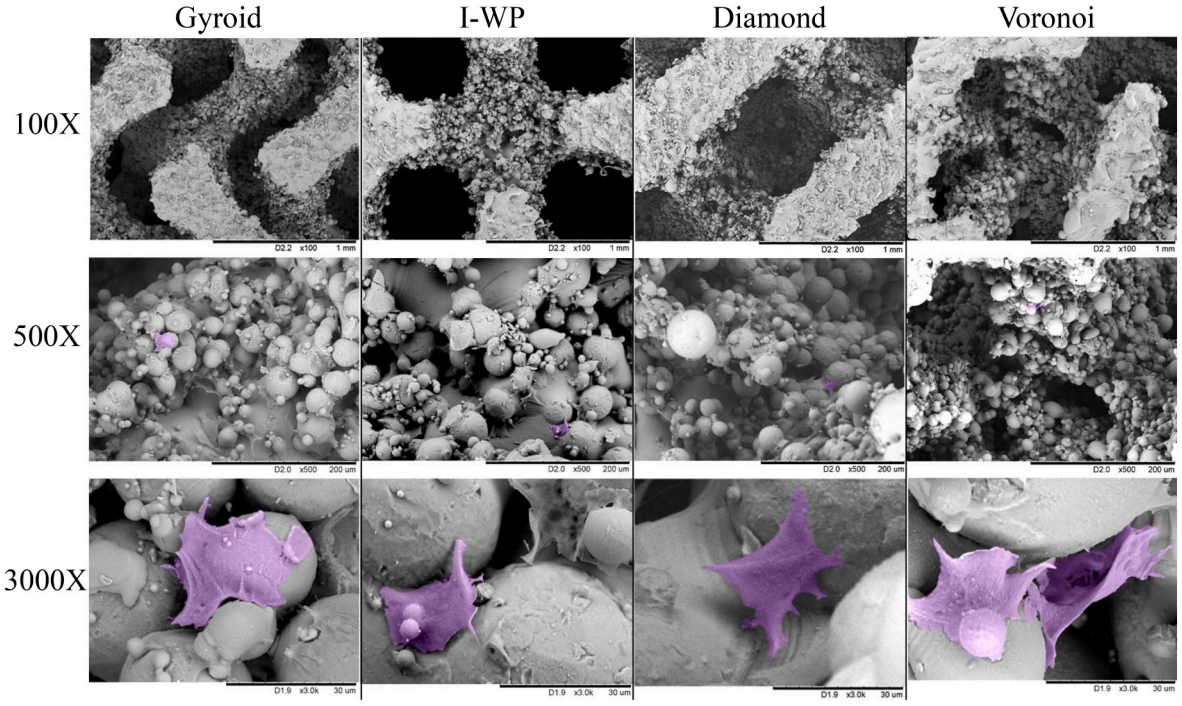

Fig. Appendices 2. Cell adhesion on each scaffold. The scalebar of the 100X is 1 mm; the scalebar of the 500X is 200 μm; the scalebar of the 3000X is 20 μm.

Table A.1
Meshed model data in the finite element analysis

	Maximum element size (mm)	Minimum element size (mm)	Number of 3D element	Number of element per volume
Gyroid	0.066	0.033	9119755	29137
I-WP	0.07	0.03	8916754	28307
Diamond	0.08	0.04	6817836	20129
Voronoi	0.07	0.03	7458919	24401

Table A.2
Primer sequences for qRT-PCR

Gene	Forward primer	Reversed primer
BMP-2	5′-AAGCGTCAAGCCAAACACAAACAG-3′	5′-GAGGTGCCACGATCCAGTCATTC-3′
ALP	5′-CTTGGTGGTCACAGCAGTTGGTAG-3′	5′-CCAGGCGACAGGTGAAGAAACAG-3′
Col1α1	5′-AACTTTGCTTCCCAGATGTCCTAT-3′	5′-CTCGGTGTCCCTTCATTCCAG-3′
Runx-2	5′-TCCCGTCACCTCCATCCTCTTTC-3′	5′-GAATACGCATCACAACAGCCACAAG-3′
OPN	5′-ATGGACGACGATGATGACGATGATG-3′	5′-CTTGTGTACTAGCAGTGACGGTCTC-3′
OCN	5′-CAAGCAGGAGGGCAATAAGGTAGTG-3′	5′-CGGTCTTCAAGCCATACTGGTCTG-3′
GAPDH	5′- GGTGAAGGTCGGTGTGAACG -3′	5′- CTCGCTCCTGGAAGATGGTG -3′

CRediT authorship contribution statement

Jialiang Li: Conceptualization, Data curation, Methodology, Writing - original draft. **Yubing Yang:** Conceptualization, Investigation, Methodology, Resources. **Zhongwei Sun:** Methodology, Software, Visualization. **Kan Peng:** Project administration, Validation. **Kaixin Liu:** Formal analysis, Methodology. **Peng Xu:** Supervision, Writing - review & editing. **Jun Li:** Visualization. **Xinyu Wei:** Methodology. **Xijing He:** Resources, Supervision, Writing - review & editing.

Declaration of competing interest

The authors declare that they have no known competing financial interests or personal relationships that could have appeared to influence the work reported in this paper.

Data availability

Data will be made available on request.

Acknowledgements

Not available.

References

[1] L. Zhang, G. Yang, B.N. Johnson, X. Jia, Three-dimensional (3D) printed scaffold and material selection for bone repair, Acta Biomater. 84 (2019) 16–33.
[2] A. Wubneh, E.K. Tsekoura, C. Ayranci, H. Uludağ, Current state of fabrication technologies and materials for bone tissue engineering, Acta Biomater. 80 (2018) 1–30.
[3] B. Wildemann, A. Ignatius, F. Leung, L.A. Taitsman, R.M. Smith, R. Pesantez, M. J. Stoddart, R.G. Richards, J.B. Jupiter, Non-union bone fractures, Nat. Rev. Dis. Prim. 7 (1) (2021) 57.
[4] A.C.Y. Loenen, M.J.M. Peters, R.T.J. Bevers, C. Schaffrath, E. van Haver, V. Cuijpers, T. Rademakers, B. van Rietbergen, P.C. Willems, J.J. Arts, Early bone ingrowth and segmental stability of a trussed titanium cage versus a polyether ether ketone cage in an ovine lumbar interbody fusion model, Spine J. 22 (1) (2022) 174–182.
[5] Y. Lai, Y. Li, H. Cao, J. Long, X. Wang, L. Li, C. Li, Q. Jia, B. Teng, T. Tang, J. Peng, D. Eglin, M. Alini, D.W. Grijpma, G. Richards, L. Qin, Osteogenic magnesium incorporated into PLGA/TCP porous scaffold by 3D printing for repairing challenging bone defect, Biomaterials 197 (2019) 207–219.
[6] Y. He, W. Wang, S. Lin, Y. Yang, L. Song, Y. Jing, L. Chen, Z. He, W. Li, A. Xiong, K. W.K. Yeung, Q. Zhao, Y. Jiang, Z. Li, G. Pei, Z.Y. Zhang, Fabrication of a bio-instructive scaffold conferred with a favorable microenvironment allowing for superior implant osseointegration and accelerated in situ vascularized bone regeneration via type H vessel formation, Bioact. Mater. 9 (2022) 491–507.
[7] Y. Yan, H. Chen, H. Zhang, C. Guo, K. Yang, K. Chen, R. Cheng, N. Qian, N. Sandler, Y.S. Zhang, H. Shen, J. Qi, W. Cui, L. Deng, Vascularized 3D printed scaffolds for promoting bone regeneration, Biomaterials 190–191 (2019) 97–110.
[8] M. Wu, F. Chen, H. Liu, P. Wu, Z. Yang, Z. Zhang, J. Su, L. Cai, Y. Zhang, Bioinspired sandwich-like hybrid surface functionalized scaffold capable of regulating osteogenesis, angiogenesis, and osteoclastogenesis for robust bone regeneration, Mater Today Bio 17 (2022), 100458.
[9] A. Salerno, A. Palladino, C. Pizzoleo, C. Attanasio, P.A. Netti, Computer-aided patterning of PCL microspheres to build modular scaffolds featuring improved strength and neovascularized tissue integration, Biofabrication 14 (4) (2022).
[10] G.E. Schroder-Turk, S. Wickham, H. Averdunk, F. Brink, J.D. Fitz Gerald, L. Poladian, M.C. Large, S.T. Hyde, The chiral structure of porous chitin within the wing-scales of Callophrys rubi, J. Struct. Biol. 174 (2) (2011) 290–295.
[11] Y. Kobayashi, R. Ohnuki, S. Yoshioka, Discovery of I-WP minimal-surface-based photonic crystal in the scale of a longhorn beetle, J R Soc Interface 18 (184) (2021), 20210505.
[12] L. Yuan, S. Ding, C. Wen, Additive manufacturing technology for porous metal implant applications and triple minimal surface structures: a review, Bioact. Mater. 4 (1) (2019) 56–70.
[13] J. Iamsamang, P. Naiyanetr, Computational method and program for generating a porous scaffold based on implicit surfaces, Comput. Methods Progr. Biomed. 205 (2021), 106088.
[14] L. Li, P. Wang, J. Jin, C. Xie, B. Xue, J. Lai, L. Zhu, Q. Jiang, The triply periodic minimal surface-based 3D printed engineering scaffold for meniscus function reconstruction, Biomater. Res. 26 (1) (2022) 45.
[15] Z. Zhao, G. Li, H. Ruan, K. Chen, Z. Cai, G. Lu, R. Li, L. Deng, M. Cai, W. Cui, Capturing magnesium ions via microfluidic hydrogel microspheres for promoting cancellous bone regeneration, ACS Nano 15 (8) (2021) 13041–13054.
[16] R. Megias, A. Vercher-Martinez, R. Belda, J.L. Peris, R. Larrainzar-Garijo, E. Giner, F.J. Fuenmayor, Numerical modelling of cancellous bone damage using an orthotropic failure criterion and tissue elastic properties as a function of the mineral content and microporosity, Comput. Methods Progr. Biomed. 219 (2022), 106764.
[17] Z. Chen, Z. Su, S. Ma, X. Wu, Z. Luo, Biomimetic modeling and three-dimension reconstruction of the artificial bone, Comput. Methods Progr. Biomed. 88 (2) (2007) 123–130.
[18] N. Sharma, D. Ostas, H. Rotar, P. Brantner, F.M. Thieringer, Design and additive manufacturing of a biomimetic customized cranial implant based on Voronoi diagram, Front. Physiol. 12 (2021), 647923.
[19] J. Li, D. Guo, J. Li, X. Wei, Z. Sun, B. Yang, T. Lu, P. Ouyang, S.e. Chang, W. Liu, X. He, Irregular pore size of degradable bioceramic Voronoi scaffolds prepared by stereolithography: osteogenesis and computational fluid dynamics analysis, Mater. Des. 224 (2022), 111414.
[20] X. Li, Y. Wang, B. Zhang, H. Yang, R.T. Mushtaq, M. Liu, C. Bao, Y. Shi, Z. Luo, W. Zhang, The design and evaluation of bionic porous bone scaffolds in fluid flow characteristics and mechanical properties, Comput. Methods Progr. Biomed. 225 (2022), 107059.
[21] S. Zou, H. Gong, J. Gao, Additively manufactured multilevel voronoi-lattice scaffolds with bonelike mechanical properties, ACS Biomater. Sci. Eng. 8 (7) (2022) 3022–3037.
[22] G. Wang, L. Shen, J. Zhao, H. Liang, D. Xie, Z. Tian, C. Wang, Design and compressive behavior of controllable irregular porous scaffolds: based on voronoi-tessellation and for additive manufacturing, ACS Biomater. Sci. Eng. 4 (2) (2018) 719–727.
[23] P. Ouyang, H. Dong, X. He, X. Cai, Y. Wang, J. Li, H. Li, Z. Jin, Hydromechanical mechanism behind the effect of pore size of porous titanium scaffolds on osteoblast response and bone ingrowth, Mater. Des. 183 (2019).
[24] F.P. Melchels, K. Bertoldi, R. Gabbrielli, A.H. Velders, J. Feijen, D.W. Grijpma, Mathematically defined tissue engineering scaffold architectures prepared by stereolithography, Biomaterials 31 (27) (2010) 6909–6916.
[25] M. Afshar, A. Pourkamali Anaraki, H. Montazerian, Compressive characteristics of radially graded porosity scaffolds architectured with minimal surfaces, Mater. Sci. Eng., C 92 (2018) 254–267.
[26] J. Li, J. Li, Y. Yang, X. He, X. Wei, Q. Tan, Y. Wang, S. Xu, S. Chang, W. Liu, Biocompatibility and osteointegration capability of beta-TCP manufactured by stereolithography 3D printing: in vitro study, Open Life Sci. 18 (1) (2023), 20220530.
[27] P.Z. Gu, Z.J. Wen, L.F. Bao, Y.B. Wang, P.R. Ouyang, T. Lu, J.L. Li, J.X. Li, M. Jiang, N. Li, X.C. Zhang, J. Wu, X.J. He, New synthetic PEKK/bioceramic hybrids and their surface sulfonation counterparts have increased cellular osteogenic capacity and promoted osseointegration, Mater. Des. 224 (2022).
[28] M. Fu, F. Wang, G. Lin, Design and research of bone repair scaffold based on two-way fluid-structure interaction, Comput. Methods Progr. Biomed. 204 (2021), 106055.
[29] S. Wang, J.M. Tarbell, Effect of fluid flow on smooth muscle cells in a 3-dimensional collagen gel model, Arterioscler. Thromb. Vasc. Biol. 20 (10) (2000) 2220–2225.
[30] X. Yuan, X. Pei, Y. Zhao, Z. Li, C.H. Chen, U.S. Tulu, B. Liu, L.A. Van Brunt, J. B. Brunski, J.A. Helms, Biomechanics of immediate postextraction implant osseointegration, J. Dent. Res. 97 (9) (2018) 987–994.
[31] M. Hollensteiner, S. Sandriesser, E. Bliven, C. von Ruden, P. Augat, Biomechanics of osteoporotic fracture fixation, Curr. Osteoporos. Rep. 17 (6) (2019) 363–374.

[32] K. Zhou, P. Yu, X. Shi, T. Ling, W. Zeng, A. Chen, W. Yang, Z. Zhou, Hierarchically porous hydroxyapatite hybrid scaffold incorporated with reduced graphene oxide for rapid bone ingrowth and repair, ACS Nano 13 (8) (2019) 9595–9606.
[33] Y. Lai, H. Cao, X. Wang, S. Chen, M. Zhang, N. Wang, Z. Yao, Y. Dai, X. Xie, P. Zhang, X. Yao, L. Qin, Porous composite scaffold incorporating osteogenic phytomolecule icariin for promoting skeletal regeneration in challenging osteonecrotic bone in rabbits, Biomaterials 153 (2018) 1–13.
[34] V. Fitzpatrick, Z. Martin-Moldes, A. Deck, R. Torres-Sanchez, A. Valat, D. Cairns, C. Li, D.L. Kaplan, Functionalized 3D-printed silk-hydroxyapatite scaffolds for enhanced bone regeneration with innervation and vascularization, Biomaterials 276 (2021), 120995.
[35] H. Fonseca, D. Moreira-Goncalves, H.J. Coriolano, J.A. Duarte, Bone quality: the determinants of bone strength and fragility, Sports Med. 44 (1) (2014) 37–53.
[36] R. Muller, Hierarchical microimaging of bone structure and function, Nat. Rev. Rheumatol. 5 (7) (2009) 373–381.
[37] P.F. Costa, A. Martins, N.M. Neves, M.E. Gomes, R.L. Reis, Automating the processing steps for obtaining bone tissue-engineered substitutes: from imaging tools to bioreactors, Tissue Eng., Part B 20 (6) (2014) 567–577.
[38] S. Gomez, M.D. Vlad, J. Lopez, E. Fernandez, Design and properties of 3D scaffolds for bone tissue engineering, Acta Biomater. 42 (2016) 341–350.
[39] A. Hoornaert, L. Vidal, R. Besnier, J.F. Morlock, G. Louarn, P. Layrolle, Biocompatibility and osseointegration of nanostructured titanium dental implants in minipigs, Clin. Oral Implants Res. 31 (6) (2020) 526–535.
[40] X. Pei, L. Wu, C. Zhou, H. Fan, M. Gou, Z. Li, B. Zhang, H. Lei, H. Sun, J. Liang, Q. Jiang, Y. Fan, X. Zhang, 3D printed titanium scaffolds with homogeneous diamond-like structures mimicking that of the osteocyte microenvironment and its bone regeneration study, Biofabrication 13 (1) (2020).
[41] K.C.R. Kolan, Y.W. Huang, J.A. Semon, M.C. Leu, 3D-printed biomimetic bioactive glass scaffolds for bone regeneration in rat calvarial defects, Int J Bioprint 6 (2) (2020) 274.
[42] E.F. Morgan, G.U. Unnikrisnan, A.I. Hussein, Bone mechanical properties in healthy and diseased states, Annu. Rev. Biomed. Eng. 20 (2018) 119–143.
[43] D.J. Hadjidakis, Androulakis, II, bone remodeling, Ann. N. Y. Acad. Sci. 1092 (2006) 385–396.
[44] G. Karsenty, S. Khosla, The crosstalk between bone remodeling and energy metabolism: a translational perspective, Cell Metabol. 34 (6) (2022) 805–817.
[45] C. Jiao, D. Xie, Z. He, H. Liang, L. Shen, Y. Yang, Z. Tian, G. Wu, C. Wang, Additive manufacturing of Bio-inspired ceramic bone Scaffolds: structural Design, mechanical properties and biocompatibility, Mater. Des. 217 (2022).
[46] H. Lei, T. Yi, H. Fan, X. Pei, L. Wu, F. Xing, M. Li, L. Liu, C. Zhou, Y. Fan, X. Zhang, Customized additive manufacturing of porous Ti6Al4V scaffold with micro-topological structures to regulate cell behavior in bone tissue engineering, Mater. Sci. Eng., C 120 (2021), 111789.
[47] X. Yao, R. Peng, J. Ding, Cell-material interactions revealed via material techniques of surface patterning, Adv. Mater. 25 (37) (2013) 5257–5286.
[48] L. Wang, X. You, L. Zhang, C. Zhang, W. Zou, Mechanical regulation of bone remodeling, Bone Res 10 (1) (2022) 16.
[49] L. Chao, C. Jiao, H. Liang, D. Xie, L. Shen, Z. Liu, Analysis of mechanical properties and permeability of trabecular-like porous scaffold by additive manufacturing, Front. Bioeng. Biotechnol. 9 (2021), 779854.
[50] J. Zhang, J. Griesbach, M. Ganeyev, A.K. Zehnder, P. Zeng, G.N. Schadli, A. Leeuw, Y. Lai, M. Rubert, R. Muller, Long-term mechanical loading is required for the formation of 3D bioprinted functional osteocyte bone organoids, Biofabrication 14 (3) (2022).
[51] A.G. Guex, J.L. Puetzer, A. Armgarth, E. Littmann, E. Stavrinidou, E.P. Giannelis, G.G. Malliaras, M.M. Stevens, Highly porous scaffolds of PEDOT:PSS for bone tissue engineering, Acta Biomater. 62 (2017) 91–101.
[52] E.J. Lee, M. Jain, S. Alimperti, Bone microvasculature: stimulus for tissue function and regeneration, Tissue Eng., Part B 27 (4) (2021) 313–329.
[53] Y. Chen, S. Zhou, J. Cadman, Q. Li, Design of cellular porous biomaterials for wall shear stress criterion, Biotechnol. Bioeng. 107 (4) (2010) 737–746.
[54] S.C. Nath, B. Day, L. Harper, J. Yee, C.Y. Hsu, L. Larijani, L. Rohani, N. Duan, M. S. Kallos, D.E. Rancourt, Fluid shear stress promotes embryonic stem cell pluripotency via interplay between β-catenin and vinculin in bioreactor culture, Stem Cell. 39 (9) (2021) 1166–1177.
[55] E.J. Arnsdorf, P. Tummala, R.Y. Kwon, C.R. Jacobs, Mechanically induced osteogenic differentiation–the role of RhoA, ROCKII and cytoskeletal dynamics, J. Cell Sci. 122 (Pt 4) (2009) 546–553.
[56] U.G. Wegst, H. Bai, E. Saiz, A.P. Tomsia, R.O. Ritchie, Bioinspired structural materials, Nat. Mater. 14 (1) (2015) 23–36.